Electronic materials

Double perovskite $Cs_2AgBiBr_6$ radiation sensor: synthesis and characterization of single crystals

Valeria Murgulov[1,*] ⓘ, Catherine Schweinle[2], Michael Daub[1,2], Harald Hillebrecht[1,2], Michael Fiederle[1], Václav Dědič[3], and Jan Franc[3]

[1] Freiburg Materials Research Center, Albert-Ludwigs-Universität Freiburg, Stefan-Meier-Str. 21, 79104 Freiburg im Breisgau, Germany

[2] Faculty of Chemistry and Pharmacy, Institute of Inorganic and Analytical Chemistry, Albert-Ludwigs-Universität Freiburg, Albert Str. 21, 79104 Freiburg im Breisgau, Germany

[3] Faculty of Mathematics and Physics, Institute of Physics, Charles University, Ke Karlovu 5, 121 16 Prague 2, Czech Republic

ABSTRACT

Single crystals of lead-free halide double perovskite $Cs_2AgBiBr_6$ sensor material manifest a remarkable potential for application in radiation detection and imaging. In this study, the purity and crystallinity of solution-grown $Cs_2AgBiBr_6$ single crystals with cubic $Fm\overline{3}m$ symmetry have been corroborated by powder XRD measurements, while the single crystal XRD patterns reveal the dominant {111} lattice planes parallel to the sample surfaces. A wider range of lower resistivity values (10^6–10^9 Ωcm) was obtained from the *I-V* measurements compared to the 1.55×10^9–6.65×10^{10} Ωcm values from the van der Pauw method, which is typically higher for the Ag than for the carbon paint electrodes. Charge-carrier mobility values estimated from the SCLC method for the carbon paint-$Cs_2AgBiBr_6$ (1.90–4.82 cm^{2}V^{-1} s^{-1}) and the Ag-$Cs_2AgBiBr_6$ (0.58–4.54 cm^{2}V^{-1} s^{-1}) including the density of trap states (10^9–10^{10} cm^{-3}) are comparable. Similar values of 1.89 cm^{2}V^{-1} s^{-1} and 2.36 cm^{2}V^{-1} s^{-1} are derived from the Hall effect measurements for a sample with carbon and Ag electrodes, respectively. The key electrical parameters including the X-ray photoresponse measurements indicate that the $Cs_2AgBiBr_6$ samples synthesized in this study satisfy requirements for radiation sensors.

GRAPHICAL ABSTRACT
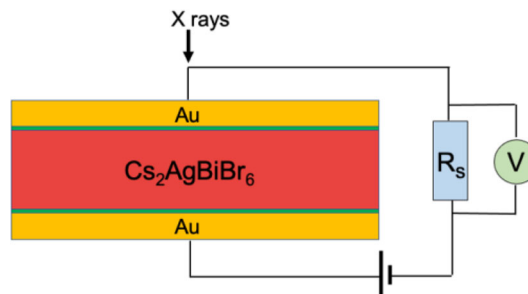
Introduction

Single crystals of hybrid methylammonium lead halide perovskite $MAPbX_3$ have demonstrated radiation detection capabilities comparable to those of the CdTe and (Cd, Zn)Te radiation sensor materials. The impressive performance of $MAPbX_3$ stems not only from its appreciably high values of resistivity ρ (10^7–10^8 Ωcm) and mobility-lifetime product $\mu\tau$ (1.2–4.1 $\times 10^{-2}$ cm^2V^{-1}) but also from low density of trap states n_{trap} (10^9–10^{10} cm^{-3}) [1–6]. However, radiation sensors with even higher ρ and $\mu\tau$ are required to enhance charge-carrier transport and collection efficiency and in turn achieve lower detection limits and higher sensitivity of devices used in X-ray security screening and medical diagnostics.

Related inorganic semiconductor material $Cs_2AgBiBr_6$ with a double perovskite structure has been proposed as a stable alternative radiation sensor due to its improved thermodynamic stability, absence of toxic lead, suppressed ion migration including a higher stopping power attributed to the heavier constituent elements. Compared to the $MAPbX_3$, single crystals of $Cs_2AgBiBr_6$ have an indirect bandgap E_G of 2.1 eV, higher ρ (10^9–10^{11} Ω cm), similar n_{trap}, modest μ (0.5–12 cm^2V^{-1} s^{-1}), lower $\mu\tau$ of 2.48–5.95 $\times 10^{-3}$ cm^2V^{-1}, and similar sensitivity of 105–1974 μCGy_{air}^{-1} cm^{-2} and detection limits of 45.7–59.7 $nGy_{air}s^{-1}$ [7–12]. These electrical and radiation detection performance parameters reflect beneficial chemical composition and crystal structure of the $Cs_2AgBiBr_6$ radiation sensor material.

$Cs_2AgBiBr_6$ belongs to the elpasolite class of materials ($A_2B^+B^{3+}X_6$) with the rock-salt arrangement of the B-crystallographic site cations in the double perovskite lattice structure described by the cubic space group $Fm\bar{3}m$, which tolerates greater substitutional flexibility than the $MAPbX_3$ [13–15]. The structure is based on a network of corner-sharing $[AgBr_6]^{5-}$ and $[BiBr_6]^{3-}$ octahedra with the Cs^+ cation at the A site (Fig. 1). A weakness in the electrical performance of $Cs_2AgBiBr_6$ has its origin in the

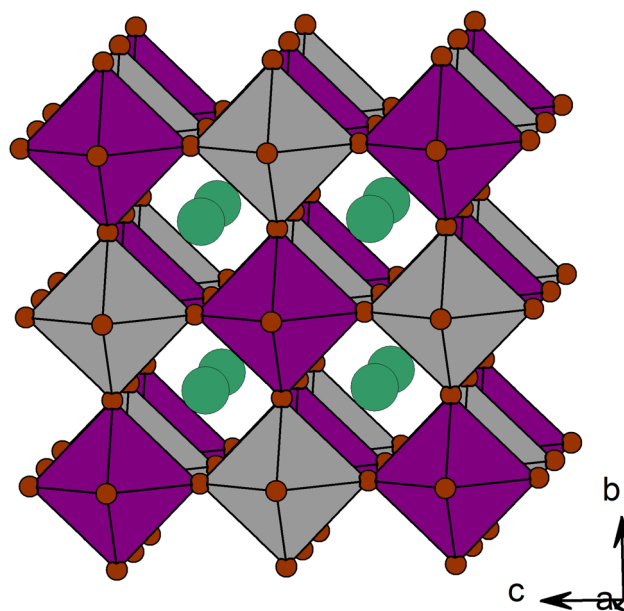**Figure 1** A unit cell of a single crystal of $Cs_2AgBiBr_6$ double perovskite. The network of corner-sharing octahedra, $[AgBr_6]^{5-}$ (grey) and $[BiBr_6]^{3-}$ (purple), with Cs cations (green) occupying the A-crystallographic sites.

electrical isolation of the two types of octahedra resulting in zero electronic dimensionality and consequently larger effective masses of charge carriers [16]. In addition, owing to the crystal structure and composition, a stronger charge carrier-lattice coupling compared to that in the $MAPbX_3$ can cause self-trapped charges and inevitably lead to limited μ [17–19]. In contrast, suppressed ion migration arising from the ordered crystal structure, stronger electrostatic interaction between the Cs^+ and Br^- including increased ion migration activation energy (348 meV) and longer ion diffusion barrier of the most mobile defect, V_{Br} (0.33 eV), permits application of a larger external bias to collect more efficiently charge carriers [7]. Indeed, enhanced charge-carrier transport is attributed to the high Ag^+/Bi^{3+} ordering along the {111} lattice planes that are orthogonal to the < 111 > direction, which is coincident with a body diagonal of the cubic lattice with a sequence of …Ag-Cs-Bi-Cs-Ag… ions. Therefore, controlled crystal growth methods are required to synthesize $Cs_2AgBiBr_6$ single crystals with the dominant {111} crystal planes.

Growth of $Cs_2AgBiBr_6$ single crystals from supersaturated low-temperature T solutions proceeds via spontaneous nucleation as the T is reduced to room T [7–9, 14, 15]. Both the energy of volume gain and the energy of nucleation growth can overcome the energy of surface increase (energy loss). Growth occurs close to the equilibrium condition and at the solid-nutrient liquid interface via transport of matter and energy. A number of growth stages, which are based on a seed dissolution-regrowth approach, are required to synthesize larger crystals whilst the equilibrium is kept in the solution and outside the nucleation region to prevent secondary nucleation. A regulated cooling crystallisation procedure permits control of the T and growth rate parameters. Development of the {111} planes is enhanced through a slow growth rate, while the {100} and {110} planes are progressively eliminated through a faster growth rate [9]. In the early stage, $Cs_2AgBiBr_6$ single crystals develop regular octahedron form {111}. Later, the growth of the $(\bar{1}11)$, $(1\bar{1}1)$, $(11\bar{1})$, $(\bar{1}\bar{1}1)$, $(\bar{1}1\bar{1})$, and $(1\bar{1}\bar{1})$ planes located at the lateral crystal faces is restricted relative to the (111) and $(\bar{1}\bar{1}\bar{1})$ planes located at the two opposite crystal faces. The final crystal form is pseudocubo-octahedral with the two largest crystal faces; one triangular face with (111) and the opposite pseudo-hexagonal face with $(\bar{1}\bar{1}\bar{1})$, which is consistent

with the $\bar{3}$-fold roto-inversion symmetry. Therefore, the size and shape of crystal faces and their angular relationships are determined not only by the shape of the unit crystal cell in the $Fm\ \bar{3}m$ but also by the crystal growth conditions such as T dependent growth rates, direction of flow of solution, and distribution of solutes at different crystal-nutrient liquid interfaces and their frequency of consumption [9].

Theoretical calculations indicate that V_{Ag} (acceptor) and Ag_i (donor) are the most important shallow defects, Bi_{Ag} (donor) is the most important deep defect, whereas V_{Br} is both a deep acceptor and a shallow donor defect [20, 21]. The trap density states present near the crystal surfaces are most likely V_{Br}; however, owing to their shallow energy ($\sim$80–90 meV) the carrier diffusion lengths exceeding 1 μm are still achievable [23]. Recent research has revealed that a Bi-poor/Br-rich growth condition can produce $Cs_2AgBiBr_6$ single crystals with suppressed density of deep electron traps Bi_{Ag} and V_{Br} [20], but this nonstoichiometry does not contribute to higher μ values [22].

A few measures have been employed to generate single crystal-based devices with enhanced performances. These include substitution of Cs^+ cations at the A-crystallographic site (e.g., phenylethylamine bromide) to improve degree of ordering $[BiBr_6]^{3-}$ and $[AgBr_6]^{5-}$ octahedra [9] and post-growth optimisation such as thermal annealing and surface cleaning with isopropanol [7], crystal cleaving [23] and optimisation of metal–semiconductor contact interfaces [24]. Despite demonstrated progress, a number of issues regarding microstructural investigation and electrical characterisation of pristine $Cs_2AgBiBr_6$ single crystals remain to be addressed.

In particular, publications do not offer insights into microstructural features of single crystals, which reflect the growth stages and progressive advances in growth conditions. They tend to focus on the space-charge-limit current (SCLC) method to derive majority of electrical performance parameters (ρ, trap-filled limit voltage V_{TFL} and in turn n_{trap} and μ) except for the $\mu\tau$ [7–9, 25]. One of the weaknesses is that the studies tend to report only the forward I-V scans, but with an inconsistent range of applied bias voltage. Another weakness is that they are limited to reporting the V_{TFL} from the intersection between the tangents of the low-voltage regime and the trap-filled-limited TFL regime. This preference overlooks an

alternative calculation from the intersection between the tangent of the space-charge-limited SCL regime and the TFL regime that can yield a more accurate value for the n_{trap} because the free charge-carrier density becomes larger than the number of traps [26]. Such weaknesses and inclinations in reporting render the correlation of key electrical parameters ambiguous. The common approach to the SCLC method has been recently reviewed and a set of recommendations for performing the *I-V* scan measurements based on experimental measurements and on drift–diffusion simulations using the MAPbBr$_3$ have been suggested [27]. We consider these remarks and proposals relevant and present a more comprehensive electrical characterisation approach to acquire the key electrical parameters on the Cs$_2$AgBiBr$_6$ radiation sensor material.

We focus on exploring advances in crystal growth through comparison of microstructural features recorded by crystals synthesised in a preliminary study with those using an advanced growth approach. Both the SCLC method and the Hall effect measurements in van der Pauw geometry are used to derive electrical performance parameters. We account for the similarities and differences in the *I-V* curves for the Ag- Cs$_2$AgBiBr$_6$ and carbon paint-Cs$_2$AgBiBr$_6$ contacts that are measured in the forward and reverse direction in the applied bias range ± 100 V. The bias in the measurements using different Keithley devices is assessed. However, variations in the determined values are clearly inevitable due to the differences in the measurement setup.

The findings of this research provide insights into the growth of red–orange $8 \times 10 \times 3$ mm^3 single crystals of Cs$_2$AgBiBr$_6$ from an assessment of microstructural features. The two opposite crystal faces (a triangular shape and a pseudo-hexagonal shape with {111} lattice planes) are consistent with the $\bar{3}$-fold roto-inversion symmetry. They are devoid of trigonal terraces, which are detrimental to charge-carrier transport. A narrower range of μ (1.89–2.36 cm^{2}V^{-1} s^{-1}) and higher range of ρ (1.55×10^9–6.65×10^{10} Ωcm) are derived from the van der Pauw and Hall effect measurements, respectively, compared to those derived from the *I-V* measurements (10^6–10^9 Ωcm and 0.58–4.82 cm^{2}V^{-1} s^{-1}) using either Ag or carbon paint electrodes. Overall, these parameters including the n_{trap} (10^9–10^{10} cm^{-3}) are in accord with the literature values. The X-ray radiation

photoresponse measurements performed on the Exp4 sample suggest suitability of all samples for radiation detection. Our studies contribute to better understanding of impressive potential of this double perovskite material in radiation detection.

Materials and methods

Initial growth of Cs$_2$AgBiBr$_6$ single crystals has in general followed the controlled cooling crystallisation method of Yin et al. [8]. Seed crystals were prepared from a boiling 66 mM solution that was cooled down to room T at 0.5 °C/h. Large crystals were grown from a 66 mM solution prepared by dissolving Bi$_2$O$_3$ (1.5184 g, ChemPur), AgBr (1.2735 g, AlfaAesar), CsBr (5.7668 g, Aldrich Chemical) in boiling HBr (100 ml 48 w%, Sigma Aldrich). A small excess of the precursor AgBr was added to suppress formation of the by-product phase Cs$_3$Bi$_2$Br$_9$. The solution was heated at 90° for 30 min to dissolve and thus smoothen the very top surfaces of the added seed crystal, and then the solution was cooled down to room T at 0.5 °C/h for 150 h in a closed oven. Successful growth of even larger crystals was achieved by adding sodium acetate NaOAc (1 equivalent, C$_2$H$_3$NaO$_2$) as an additive [28]. This growth method yielded higher-quality red–orange, semitransparent Cs$_2$AgBiBr$_6$ single crystals ca. $8 \times 10 \times 3$ mm^3 with a pseudocubo-octahedral form and smoother pseudo-hexagonal crystal faces.

Characterisation techniques

A digital microscope Keyence VHX-5000 and a differential interference contrast microscope Zeiss Axio Imager that operates in reflected light and in transmitted light, respectively, were used to examine microstructures of the synthesized single crystals.

The powder X-ray diffraction (PXRD) data were collected using the STOE STADI P transmission diffractometer. This device is equipped with filtered Mo-$K_{\alpha 1}$ radiation (λ of 0.7093 Å), curved Ge (111) monochromators, and the MYTHEN 1 K silicon microstrip detector. The setup included the Debye–Scherrer scan mode, a fixed sample, and the detector. The processing of data was performed using the STOE WinX^{POW} software program.

Single-crystal XRD *2θ* scan measurements were obtained using the Bruker D8 Discover

diffractometer. This device features a high-resolution Cu-$K\alpha$ radiation source (λ of 1.54060 Å $K\alpha_1$ and λ of 1.54439 Å $K\alpha_2$), a focusing Goebel mirror as the primary monochromator including an 18 mm anti-scatter slit and a 0.5 mm divergence slit in a fixed mode, and a line focus silicon strip detector LynxEye Xe. The generator was set to 40 mA and 40 kV. The XRD data acquisition and processing were performed using the Bruker Diffrac.EVA software® and the Crystal Impact Match! software.

Electrical characterisation measurements were performed using the Keithley source meter unit (SMU) 2450, an electrometer 6517B model, and a shielded test fixture model 8101 4TRX to minimise electrostatic interferences by shielding and to control leakage current in the cables and connectors by guarding. The purpose of the electrical characterisation was two-fold. The I-V measurements were carried out to determine whether the Ag glue-$Cs_2AgBiBr_6$ and Plano® carbon paint-$Cs_2AgBiBr$ contacts exhibit the ohmic behavior and to calculate the values of ρ, V_{TFL} and estimate the values of μ and n_{trap}. The van der Pauw method and the Hall effect measurements were performed to assess the SCLC derived ρ and μ values and to determine the charge-carrier type and its concentration (n, p).

The X-ray photoresponse measurements were carried out using the X-ray tube with a beam source of the RQR6 quality (tungsten target, voltage 80 kV, 1 mm thick Be, and 2.9 mm thick Al filters). Au electrodes were deposited by evaporation on the two opposite crystal faces of the selected sample Exp4 using a few nm thick adhesive Cr layer. The front Au electrode was irradiated while a fixed bias was applied to the front and back electrodes to extract the charges generated by the photoelectric effect. The photocurrent measurements were taken after 1 min with the bias set to ± 2 V and -10 V and were determined indirectly using a serial resistor R_s (100 MΩ) due to the very high resistivity of the sample. The measured current values are in the pA-range and have an error estimated to 5% at higher X-ray dose rates when the voltage across the sample can drop by 5% to 10%. This fact, however, did not affect the qualitative evaluation of the sample response. The estimated errors (relative) in the measurements are in the range 2–5%.

Data treatment: electrical characterisation

SCLC is commonly employed to interpret I-V characteristics and determine charge-carrier transport parameters of single-carrier devices [29–31]. The I-V curves were measured in a 0 V to $\pm$ 100 V bias range, for a forward scan (top crystal face T (+) bottom crystals face B (−) configuration) and for a reverse scan (T (−) B (+) configuration), with a source delay time set to 0 s, 5 s, 10 s, 15 s, 20 s and 25 s between voltage steps of 1 V and 3 min between the change of applied bias direction. The Ag glue and Plano® carbon electrodes were deposited on the two opposite crystal faces (Supplementary Information Fig. S1a). The area of Ag glue and carbon paint electrodes deposited on a crystal surface was estimated to 0.0227 cm². It was assumed that the contacts do not inject charge carriers at the applied voltages.

In principle, in a low-voltage range, I-V curves follow Ohm's law (a linear dependence of I on V). In a mid-voltage range, a trap-filled (TFL) regime develops due to the presence of electronic trap states and the I-V curves in a log–log plot have a slope of more than 2 [32]. The n_{trap} is calculated from the equation:

$$V_{TFL} = q n_{trap} L^2 / \varepsilon_o \varepsilon_r$$

where L is the thickness, and ε_o and ε_r are the vacuum and relative dielectric constants, respectively [33]. In a high-voltage range, a trap-free regime develops due to filling of the traps with the injected free carriers and consequently, the current is limited by the build-up of space-charge. The I-V curves in a log–log plot have a slope of 2 [29]. The current density follows the Mott-Gurney law:

$$J = (9/8)\mu\varepsilon_o\varepsilon_r(V)^2 / L^3$$

where $V = V_{TFL}$; hence,

$$\mu = (8/9)JL^3 / V_{TFL}^2 \varepsilon_o \varepsilon_r$$

.

Most publications report the V_{TFL} calculated from the crossing point between the tangent of the Ohmic I-V curve and the TFL I-V curve, which is then used to estimate the value of n_{trap}. However, a more accurate value can be obtained from the V_{TFL} at the crossing point between the SCLC I-V curve and the TFL I-V curve [26]. From the I-V measurements conducted at different source delay times, it is inferred that the I-V curves measured at 20 s delay

Figure 2 Images of crystal microstructures obtained in reflected▶ light (colored images) and in transmitted light (black and white images). The top crystal face of the Exp0 sample has a triangular shape with three distinct edges instead of sharp corners. It is characterised by pronounced facets and trigonal terraces (**a**). The bottom face with a pseudo-hexagonal shape has neither facets nor terraces (**b**). The triangular face of the Exp2 exhibits minor step-growth and dissolution features including localised strained lattice in the vicinity of the seed (**c–d**), while the pseudo-hexagonal face shows mainly precipitates (**e**).

time is sufficient to reveal the three regimes required to estimate reliable ρ, V_{TFL}, μ, and n_{trap} values using the SCLC method.

For the van der Pauw method, the Ag glue and the carbon paint electrodes were deposited on a hexagonal-shaped crystal face as shown in the Supplementary Information Fig. S1b. The preliminary Hall-effect measurements on the sample Exp4 were performed in van der Pauw geometry by applying a magnetic field $\vec{B}_z$ of 0.85 T perpendicular to sample's surface. From these measurements, the n and p, μ, and the charge-carrier type were determined. To reduce the effect of biasing and to validate the recorded values, several measurements were performed using the Keithley model 6517B electrometer and the SMU 2450 in different configurations (a voltmeter, an ammeter, and a voltage/current source). All *I-V*, van der Pauw, and Hall effect measurements were repeated at least twice to ensure stability of the Keithley devices and reproducibility of the recorded values, and in turn to increase reliability of calculated values.

The Struer's GmbH MD-Nap polishing pad, DP-lubricant yellow, and aerosol DP-P spray ¼ µm were used to mechanically remove the Ag glue and carbon paint electrodes from the surfaces of the $Cs_2AgBiBr_6$ crystals. The crystals were then washed in isopropanol.

Results

Microstructure

Initial crystal growth yielded pseudocubo-octahedral single crystals of $Cs_2AgBiBr_6$ with an average size of $5 \times 5 \times 1.5$ mm^3. All samples have a top crystal face with a triangular shape and the opposite bottom face
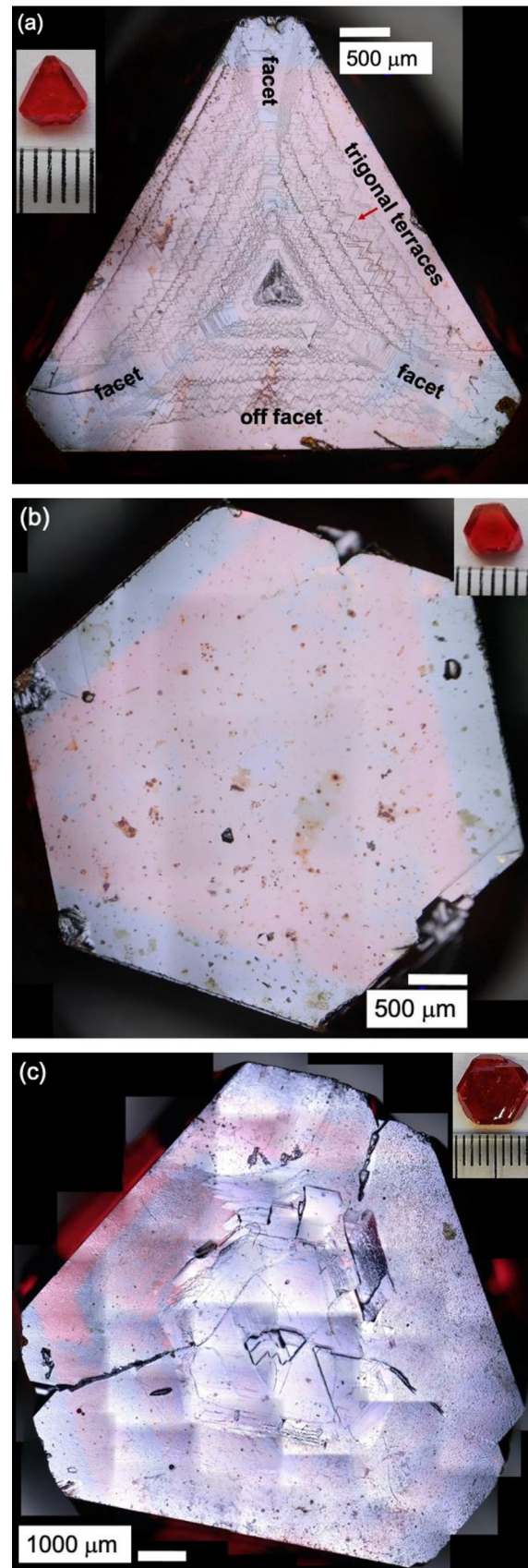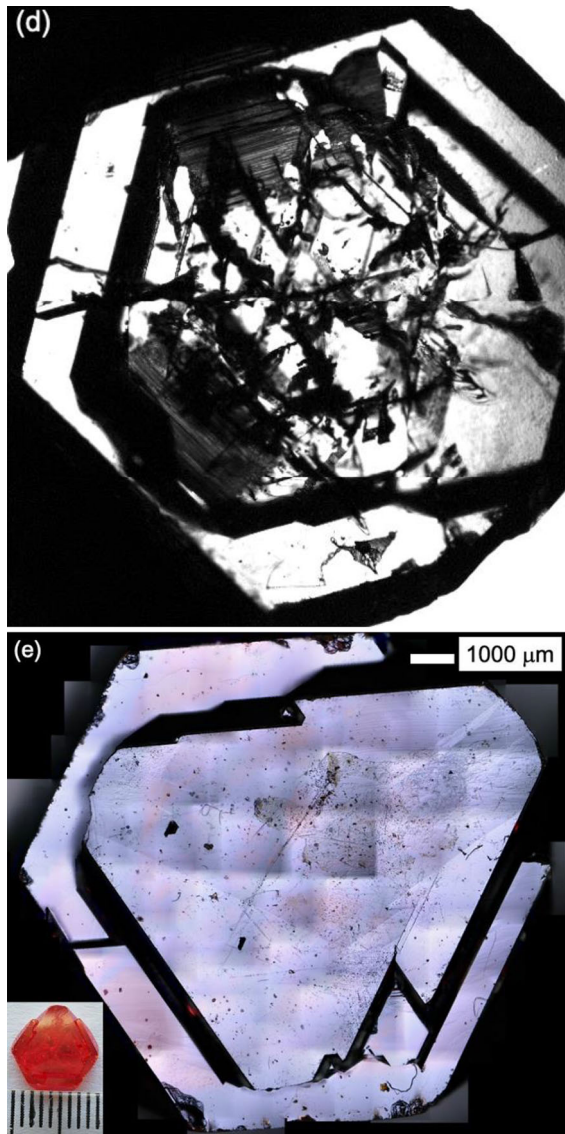
Figure 2 continued.

with a pseudo-hexagonal shape (Fig. 2a; Exp0) consistent with a $\bar{3}$-fold roto-inversion symmetry along the < 111 > growth direction in the cubic lattice ($Fm\bar{3}m$). The triangular face exhibits prominent (111) facets at 120° and off-facet regions that reflect a free growth, but intermittent stages of growth and dissolution (dark grey to black striations) as a consequence of a variable T gradient. In the off-facet regions, trigonal terraces appear in variable intensity and distribution with narrower and wider spaced striations developed due to slower growth rates and faster rates, respectively. These pronounced nonsymmetrical features produce not only a rougher crystal surface and a non-uniform sample thickness

but evidently, degrade electrical performances. The opposite face with a pseudo-hexagonal shape and $\bar{3}$-fold roto-inversion symmetry is defined by the edges that have been formed through the intersection between alternating opposite and inclined other crystal faces. It has neither facets nor terraces (Fig. 2b; Exp0). Instead, it is riddled with numerous circular and rectangular-shaped impurities (e.g., solvated precursor ions). In general, unstable crystal-solution interfaces cause incorporation of impurities into the growing crystal that can cluster to form precipitates
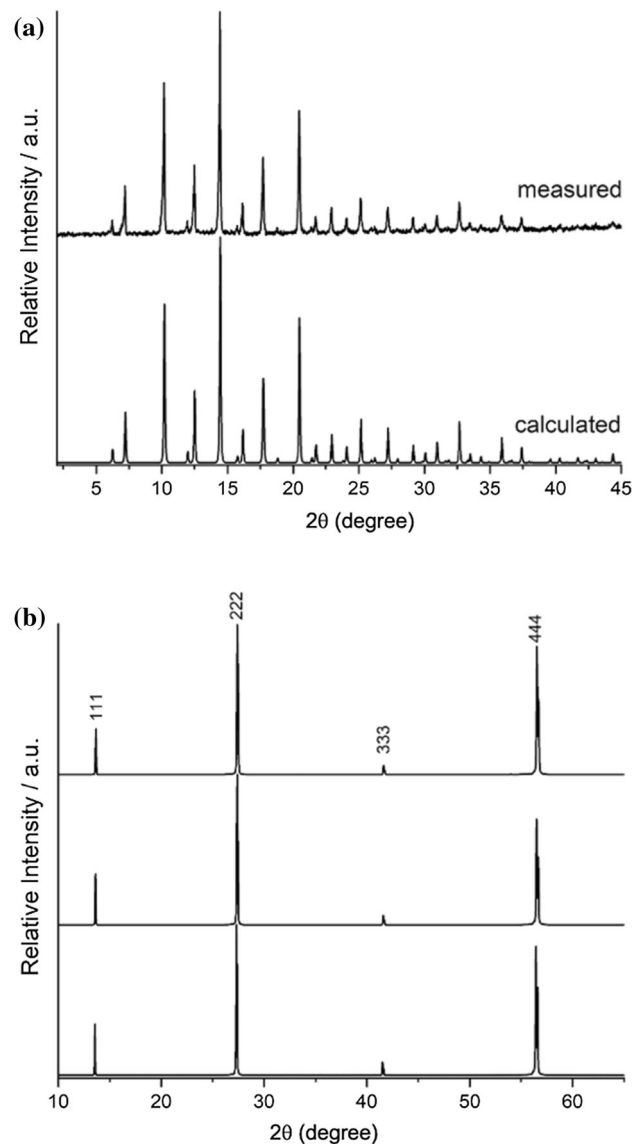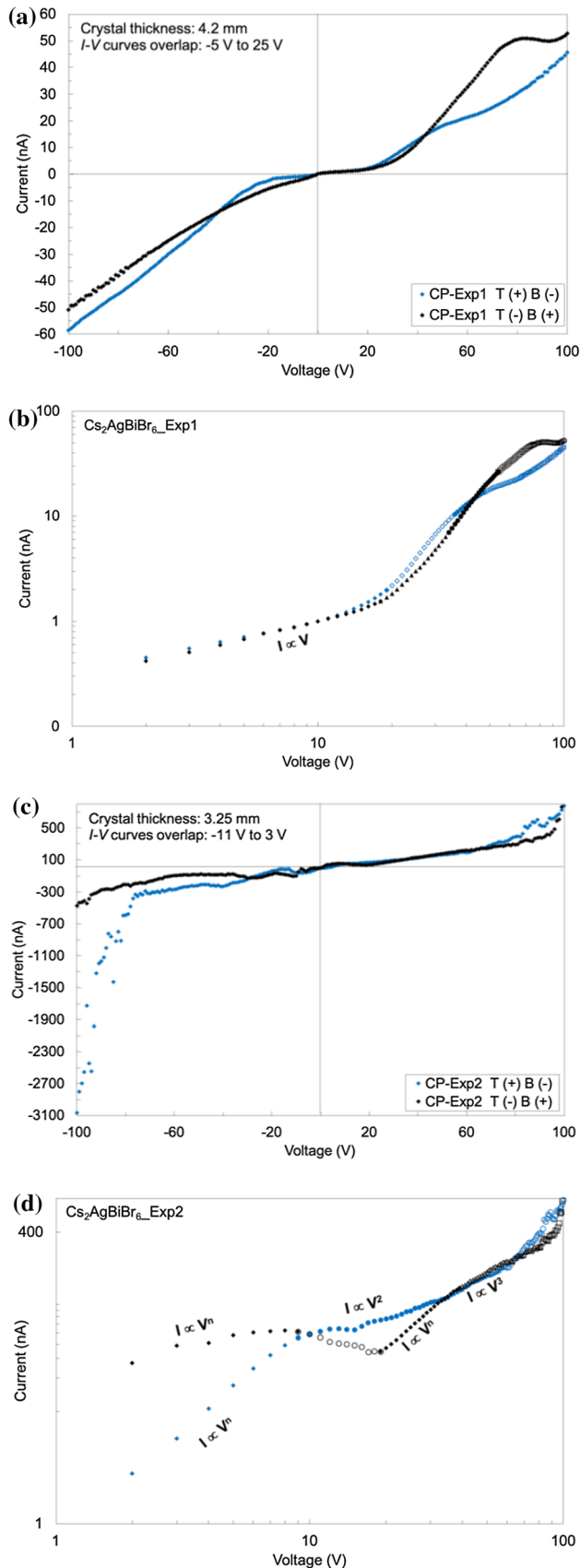

Figure 3 PXRD pattern (Mo-$K\alpha_1$ radiation source) for the Cs$_2$AgBiBr$_6$ powder samples (**a**) and the XRD patterns (Cu-$K\alpha_1$ radiation source) for the single crystals Exp1, Exp2, and Exp3 from bottom to top (**b**).

◀**Figure 4** *I-V* curves generated in the dark for the carbon paint-Cs$_2$AgBiBr$_6$-carbon paint vertical device: the forward scan T (+) B (−) blue and the reverse scan T (−) B (+) black). The log–log plots show the identified charge-carrier transport regimes (**b**, **d**, **f**, **g**). No TFL regime and no SCLC regime can be identified in the log–log plot for the carbon paint-Exp1 (**b**). In the 4f, the gradient for the 25–47 V range is 1.17 (V^1), while the gradient for the 47–100 V range is 2.88 (V^3).

as a consequence of its growth on the bottom of a growth vessel.

The improved crystal growth produced larger crystals (8 × 10 × 3 mm^3) with flatter and smoother surfaces. Relative to the samples Exp2 and Exp3, the samples Exp1 and Exp4 are more tabular. The two largest and opposite crystal faces are flat and as such desirable for electrical characterisation and X-ray photoresponse measurements. These surfaces are devoid of pronounced trigonal terraces (e.g., Exp2; Fig. 2c–d). However, all samples have strained and fractured overgrowth zones due to stress imparted by a seed (Supplementary Information; e.g., Figure S2a and S2g–h), and some exhibit twin planes (Supplementary Information; e.g., Figure S2e).

Crystal structure

The phase purity (absence of the precursors and extrinsic dopants) and crystallinity of all Cs$_2$AgBiBr$_6$ samples have been verified from the PXRD data (Fig. 3a). The refined unit-cell parameters $a = b = c = 11.2773$ (7) Å, $\alpha = \beta = \gamma = 90°$ and the unit cell volume of 1434.22 (14) Å^3 are consistent with the cubic crystal system and the $Fm\overline{3}m$. The data are given in Supplementary Information (Table S1). High ordering of Ag$^+$ and Bi^{3+} octahedra cations is apparent from the XRD patterns for single crystals that depict peaks arising solely from the {111} family of planes (Fig. 3b).

Refinement of the single crystal data yielded lattice parameter value of $a = b = c = 11.2548$ (7) Å and the unit cell volume of 1425.6 4(16) Å^3, which proves the excellent data quality (Supporting Information; Table S2).
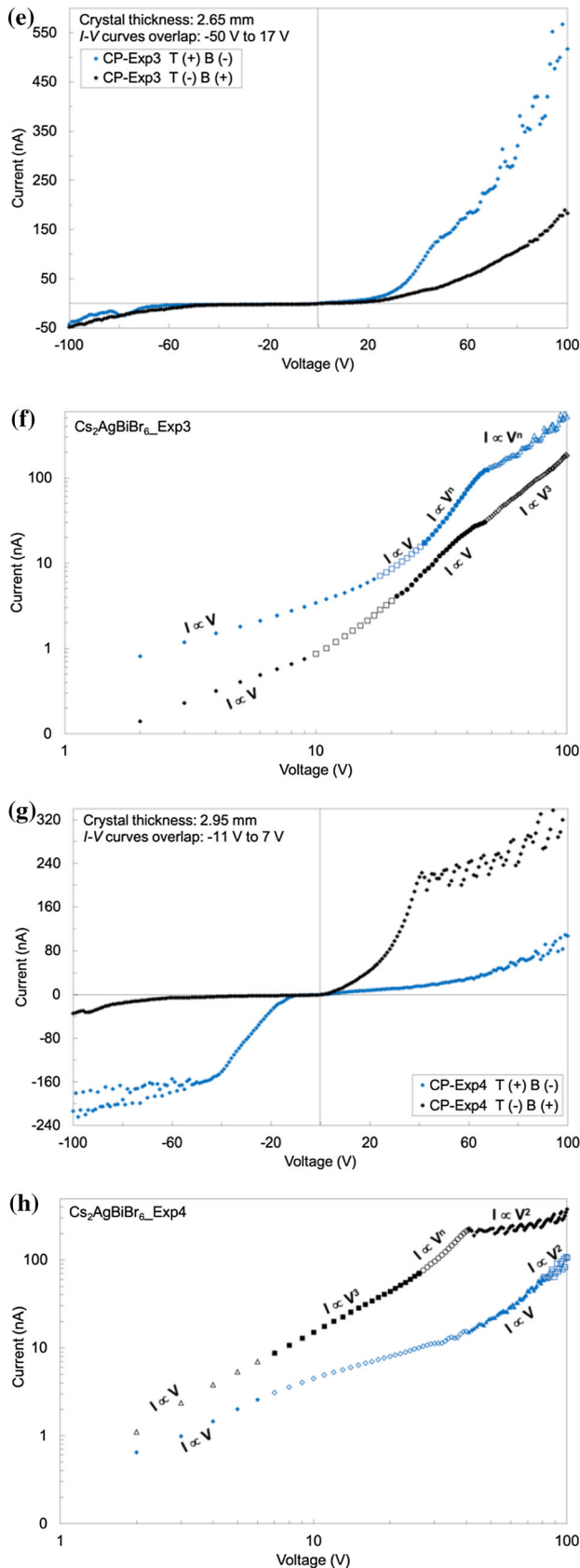
Figure 4 continued.

Electrical characterisation

I-V measurements

The *I-V* scans for the carbon paint-$Cs_2AgBiBr_6$ are symmetrical in the low voltage range but fluctuate in the high voltage range (Fig. 4). The overlapping ohmic regimes range from −11 to 3 V for the sample Exp2 with the ρ of 10^6–10^7 Ωcm, to −50 V to 17 V for the Exp3 with the ρ of 5.88–9.23 × 10^8 Ωcm (Table 1). Also, the maxima levels of the measured current over the whole bias range for the carbon paint-Exp2 and carbon paint-Exp3 contacts (Fig. 4c and e) are unequal and the shape of the *I-V* curves does not mirror those of the carbon paint-Exp1 and carbon paint-Exp4 contacts (Fig. 4a and g).

In the mid-to high-voltage range, the overlapping ohmic, TFL, and SCLC regimes of the *I-V* curves for the carbon-Exp1 (Fig. 4b) preclude clear identification of the V_{TFL} and in turn calculation of μ and n_{trap}; hence, the values can be estimated only with reference to other samples (Table 1). The forward *I-V* scan for the carbon-Exp2 has both the SCLC and TFL regimes (Fig. 4c). The μ of 160.6 cm^2V^{-1} s^{-1} at V_{TFL} of 9.17 V is overestimated and the n_{trap} is 4.89 × 10^9 cm^{-3} is underestimated. The more realistic values of 27.5 cm^2V^{-1} s^{-1} and 1.76 × 10^{10} cm^{-3} have been calculated at V_{TFL} of 32.9 V. Only the TFL regimes can be identified in the *I-V* scans of the carbon-Exp3 (Fig. 4e; Table 1). The TFL and SCLC regimes of the reverse *I-V* scan for the carbon Exp4 yield 38.1 cm^2V^{-1} s^{-1} and 5.14 × 10^9 cm^{-3} at V_{TFL} of 7.94 V and 28.9 cm^2V^{-1} s^{-1} and 2.47 × 10^{10} cm^{-3} at V_{TFL} of 38.1 V. The forward scan has the linear and SCLC regimes in the mid-to high-voltage range (Fig. 4h); hence, the μ and n_{trap} values are estimated (Table 1).

Reasonably symmetrical *I-V* curves for the Ag-$Cs_2AgBiBr_6$ were obtained over the applied bias range in both forward and reverse scan directions (Fig. 5). In the low-voltage range, where the curves overlap, the contacts exhibit the ohmic behavior. The narrowest overlap is from −10 to 4 V for the Exp1 and Exp2 samples with the ρ of 1.02 × 10^8–1.08 × 10^9 Ωcm (Fig. 5a and c; Table 2), whereas the widest range is from −60 to 10 V for the Exp3 (Fig. 4e) with the ρ of 1.74–2.97 × 10^9 Ωcm (Table 2). The maximal values of the measured current for the Ag-Exp2 and Ag-Exp3 contacts (Fig. 5c and e) are neither equal to nor does the shape of the *I-V* curves mirror those of

Table 1 Calculated ρ, $\boldsymbol{\mu}$ and $\boldsymbol{n_{trap}}$ from the I-V curves for the $Cs_2AgBiBr_6$ sample using Plano® carbon paint electrodes

Sample	Contacts	L (mm)	U (V)	$\rho(\Omega cm)$	V_{TFL}(V)	μ (cm^{2}V^{-1}s^{-1})	n_{trap}(cm^{-3})
Exp1	T + B −	4.20	− 5 to 25	4.02×10^8	28.6	4.82	1.52×10^{10}
	B + T −			4.19×10^8	34.2	3.84	1.83×10^{10}
Exp2	T + B −	3.25	− 11 to 3	1.09×10^7	9.17	160.6	4.89×10^9
					32.9	27.45	1.76×10^{10}
	B + T −			6.93×10^6	3.40		1.18×10^9
Exp3	T + B −	2.65	− 50 to 17	5.88×10^8	29.5	4.50	2.37×10^{10}
	B + T −			9.23×10^8	54.2	2.41	2.89×10^{10}
Exp4	T + B −	2.95	− 11 to 7	2.73×10^8	75.5	1.90	5.02×10^{10}
	B + T −			1.17×10^8	7.94	38.1	5.14×10^9
					38.10	28.9	2.47×10^{10}

Sample thickness L; Trap filled limit voltage V_{TFL}; density of trap states n_{trap}; resistivity ρ; Ohmic voltage range U; permittivity of vacuum ε_o of 8.85×10^{-14} Fcm^{-1}; relative permittivity of $Cs_2AgBiBr_6$ ε_r of 51 [7]; elementary charge q of 1.602176×10^{-19} Ce^{-1}. The resistivity values are calculated from the most linear segment along the I-V curve and where the curves for the forward and the reverse scans overlap. Area of the contacts 0.0227 cm^2. Top trigonal crystal face T; Bottom pseudo-hexagonal crystal face B

the Ag-Exp1and Ag-Exp4 contacts (Fig. 5a and g). In the mid-to high-voltage range, the I-V curves in both scan directions are characterised by fluctuations.

The absence of distinctive TFL and SCLC regimes preclude clear definition of the V_{TFL}, especially for the Ag-Exp1, and in turn calculation of the μ and n_{trap} (Fig. 5a and b; Table 2). In contrast, the SCLC and TFL regimes of the I-V scans for the Ag-Exp2 are well defined for both scans (Fig. 5c and d). For the forward I-V scan, the estimated μ at V_{TFL} of 8.33 V is 24.4 cm^{2}V^{-1} s^{-1} and the n_{trap} is 4.44×10^9 cm^{-3}, whereas at V_{TFL} of 17.0 V the μ is 22.9 cm^{2}V^{-1} s^{-1} and the n_{trap} is 9.08×10^9 cm^{-3}. The lower μ (2.82 cm^{2}V^{-1} s^{-1} and 4.54 cm^{2}V^{-1} s^{-1}) and the higher n_{trap} (1.79×10^{10} cm^{-3} and 2.26×10^{10} cm^{-3}) were calculated for the reverse scan at V_{TFL} of 33.6 V and 42.4 V, respectively (Table 2). Better defined SCLC regimes and more reliable estimates for the V_{TFL} and in turn, the μ of 0.58 cm^{2}V^{-1} s^{-1} and 3.08 cm^{2}V^{-1} s^{-1} and the n_{trap} of 3.44×10^{10} cm^{-3} and 8.50×10^9 cm^{-3} were obtained for the reverse scans of the Ag-Exp3 and Exp4, respectively (Fig. 5e–h; Table 2).

Notable differences identified between the Ag-$Cs_2AgBiBr_6$ and carbon paint-$Cs_2AgBiBr_6$ contacts include the current maxima values over the entire range of applied bias and the shape of the I-V curves. The data scattering is more prominent in case of the carbon-Exp2, Exp3, and Exp4, and the Ag-Exp1 and Ag-Exp2. The carbon-Exp3 and Ag-Exp3 exhibit saturation in current at low values for both scan

directions in the negative bias range, while there is a significant mismatch in the current maxima recorded by the Ag-Exp3 for the two scan directions under positive bias range. Both contacts also share a number of key features. The ohmic range is similar, the three segments are absent in the log–log plots of I-V curves for the sample Exp1, while the Exp1 and Exp4 exhibit similar maxima current levels. In general, the Ag-$Cs_2AgBiBr_6$ contacts are more resistive than the carbon paint-$Cs_2AgBiBr_6$ and yield slightly lower μ, but similar n_{trap}.

Van der pauw method and hall-effect measurement results

The highest ρ values for both the Ag-$Cs_2AgBiBr_6$-Ag and the carbon-$Cs_2AgBiBr_6$-carbon configurations are on the order of 10^{10} Ωcm, with the maximum value of 6.65×10^{10} Ωcm calculated for the Ag-Exp4. These values were determined from the measurements using the 6517B as a voltage source (5 V or 10 V) and an ammeter in combination with the SMU 2450 as a voltmeter and also from the measurements using the SMU 2450 in the constant current mode (1 nA or 2 nA) (Table 3). At higher bias (20 V) and current (10–20 nA) values, the charges are injected at the electrode interfaces and ρ values are reduced to 10^9 Ωcm. The samples contacted with Ag electrodes demonstrate higher resistivity and, hence, a more efficient electrical performance. The preliminary Hall-effect measurements yielded the μ and p values of 1.89 cm^{2}V^{-1} s^{-1} and 1.10×10^{10} cm^{-3} for the

(a)

Crystal thickness: 4.2 mm
I-V curves overlap: -10 V to 4 V

- Ag-Exp1 T (+) B (-)
- Ag-Exp1 T (-) B (+)

(b)

$Cs_2AgBiBr_6$_Exp1

(c)

Crystal thickness: 3.25 mm
I-V curves overlap: -10 V to 4 V

- Ag-Exp2 T (+) B (-)
- Ag-Exp2 T (-) B (+)

(d)

$Cs_2AgBiBr_6$_Exp2

$I \propto V^3$
$I \propto V^2$
$I \propto V$
$I \propto V^2$
$I \propto V^n$
overlappling $I \propto V$ and $I \propto V^n$
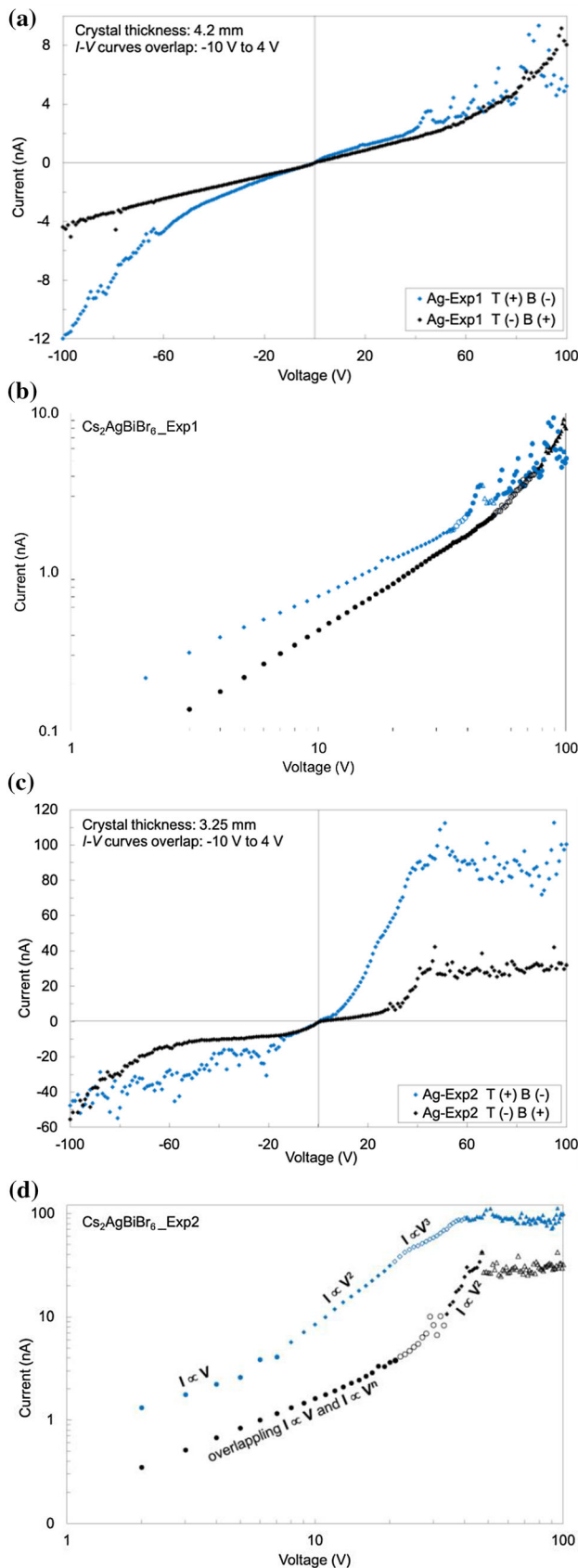
◀ **Figure 5** *I-V* curves generated in the dark for the Ag-$Cs_2AgBiBr_6$-Ag vertical device: the forward scan T (+) B (−) blue and the reverse scan T (−) B (+) black). The log–log plots show the identified charge-carrier transport regimes (**b**, **d**, **f**, **g**). No TFL regime and no SCLC regime can be identified in the log–log plot for the Ag-Exp1 (**b**).

carbon-Exp4 and 2.36 $cm^2V^{-1} s^{-1}$ and 1.15×10^{10} cm^{-3} for the Ag-Exp4.

X-ray photoresponse

A plot of calibration data is shown in Fig. 6a. An almost linear dependence of the photocurrent density on the dose rate can be observed for the fixed bias of ± 2 V and −10 V, with higher values at −10 V (Fig. 6b). When the detector is biased to −10 V, its maximum sensitivity is 42 μCGy_{air}^{-1} cm^{-2} at a dose rate of 75 μGys^{-1}. The relationship between the sample photocurrent density and the bias voltage from −20 to 20 V has been determined by fixing the X-ray tube current to 5 mA and the sample-to-source distance to 1000 mm (Fig. 6c). The *I-V* curve is in general symmetrical over the voltage range.

Discussion

A number of important differences between the crystals synthesized during a preliminary study and those using a more advanced approach indicate an overall improvement in crystal growth method. Obviously, the crystal size has doubled and surfaces are smoother and flatter. However, the most evident microstructural improvement is the absence of prominent trigonal growth terraces with narrower and wider spaced striations, which reflect slower and faster growth rates, respectively. These features including strained crystal lattice and defects degrade crystal quality and as such have an evident impact on the electrical performance. A regulated crystal growth of $Cs_2AgBiBr_6$ single crystals requires controlling the crystal growth parameters and consequently the stability of crystal-nutrient interface. A too high T rate results in a higher concentration of defects, whereas a too low T rate promotes secondary nucleation. A fast growth rate introduces defects and morphological instability due to kinetic processes at the crystal-nutrient interface, whereas a slow growth
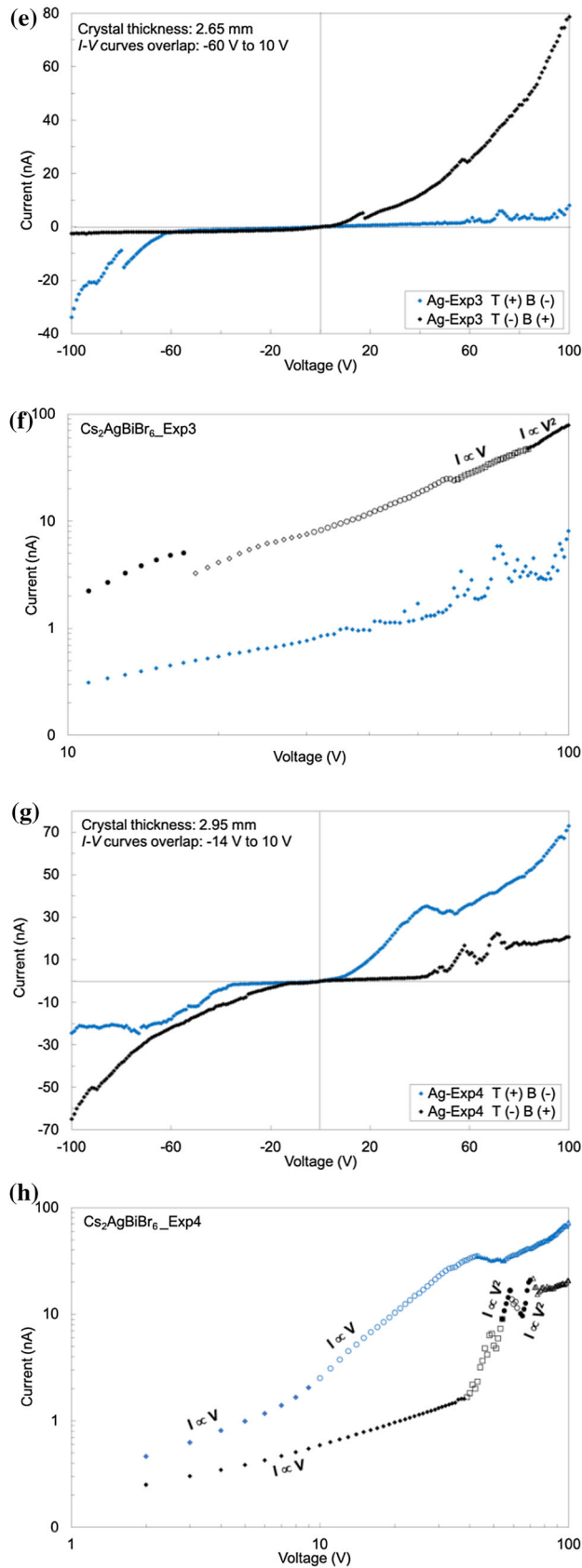
Figure 5 continued.

rate causes formation of volume defects due to clustering of vacancies/interstitials, dislocations, and plane defects, or formation of precipitates. Further improvements in crystal growth are required to increase the size and reduce density of defects in crystals. The PXRD and the single crystal XRD measurement results are in accord with the literature [7–10, 14, 15].

With regard to electrode type used for contacting purposes, typically Au is evaporated on the opposite crystal faces of a $Cs_2AgBiBr_6$ single crystal [7]. The electrode work function ϕ and whether it matches the conduction band E_C or the valance band E_V of a semiconductor has an impact on the dominant charge-carrier transport [31]. Hence, Au with ϕ_{Au} of 5.10–5.47 eV matches more closely the E_V of the $Cs_2AgBiBr_6$ at 5.64 eV [24] and the Au-$Cs_2AgBiBr_6$-Au has been reported as a weakly p-type (hole-only devices) [7]. In this study, Ag glue and Plano® carbon paint electrodes were used. The Ag electrode ϕ_{Ag} of 4.26 eV matches the E_C of the $Cs_2AgBiBr_6$ at 3.64 eV [24], thus, the Ag-$Cs_2AgBiBr_6$-Ag is an electron-only device. The carbon paint ϕ_{CP} of ca. 4.62 eV matches both the E_C (0.98 eV) and the E_V (1.02 eV) of $Cs_2AgBiBr_6$ resulting in a double-carrier carbon paint-$Cs_2AgBiBr_6$-carbon paint device. Because the Fermi energy E_F of Ag is close to the E_F of $Cs_2AgBiBr_6$, which is at 4.852 eV, injection barrier $q\phi_{inj}$ at the interface can form [30]. However, the effect of $q\phi_{inj}$ on the Ag-$Cs_2AgBiBr_6$-Ag and carbon paint-$Cs_2AgBiBr_6$-carbon paint devices is considered low, because of the sample thicknesses (2.65–4.2 mm).

The mismatch in the current maxima values of the measured I-V curves for the Exp2 and Exp3 over the whole applied bias range (Fig. 4c and e; Fig. 5c and e) do not imply rectifying contacts, because this feature is characteristic for both the Ag and carbon paint electrodes. There is no unique justification to account for this inconsistency. In terms of the nature of samples, both the Exp2 and Exp3 have thinner rims than the centers, where the seed is located. The overgrowth zones grew as unsymmetrical vertical stairs and developed not only uneven surfaces but also variable defect densities (e.g., twin boundaries, dislocations, inclusions, and impurities). Another possible explanation is a surface-conduction effect. However, the possibility of formation of an injection barrier associated with degradation of the double

Table 2 Calculated values for the ρ, μ and n_{trap} from from the I-V curves for the Cs$_2$AgBiBr$_6$ samples using Ag glue electrodes

Sample	L (mm)	Contacts	U (V)	$\rho(\Omega cm)$	V_{TFL}(V)	μ (cm^{2}V^{-1}s^{-1})	n_{trap}(cm^{-3})
Exp1	4.20	T + B −	− 10 to 4	8.13×10^8	35.0		1.87×10^{10}
		B + T −		1.08×10^9	51.0		2.72×10^{10}
Exp2	3.25	T + B −	− 10 to 4	1.02×10^8	8.33	24.4	4.44×10^9
					17.0	22.9	9.08×10^9
		B + T −		1.20×10^8	33.6	2.82	1.79×10^{10}
					42.4	4.54	2.26×10^{10}
Exp3	2.65	T + B −	− 60 to 10	2.97×10^9	67.9	0.07	3.62×10^{10}
		B + T −		1.74×10^9	15.9	3.08	8.50×10^9
					84.7	1.14	6.79×10^{10}
Exp4	2.95	T + B −	− 14 to 10	9.18×10^8	14.9	2.05	7.96×10^9
		B + T −		8.19×10^8	53.2	0.58	3.44×10^{10}
					66.5	0.64	4.31×10^{10}

Sample thickness L; Trap filled limit voltage V_{TFL}; density of trap states n_{trap}; resistivity ρ; Ohmic voltage range U; permittivity of vacuum ε_o of 8.85×10^{-14} Fcm^{-1}; relative permittivity of Cs$_2$AgBiBr$_6$ ε_r of 51 [7]; elementary charge q of 1.602176×10^{-19} Ce^{-1}. The resistivity values are calculated from the most linear segment along the I-V curve and where the curves for the forward and the reverse scans overlap. Area of the contacts 0.0227 cm^2. Top trigonal crystal face T; Bottom pseudo-hexagonal crystal face B

Table 3 ρ values for the Cs$_2$AgBiBr$_6$ samples with Ag glue and carbon paint electrodes

$\rho(\Omega cm)$

Setup	Exp1-Ag	Exp2-Ag	Exp3-Ag	Exp4-Ag	Exp1-carb	Exp2-carb	Exp3-carb	Exp4-carb
3a	4.88×10^{10}	2.73×10^{10}	4.39×10^{10}	5.40×10^{10}	7.37×10^9	7.50×10^9	5.09×10^9	5.52×10^9
3b	3.51×10^{10}	2.34×10^{10}	2.67×10^{10}	6.65×10^{10}	3.55×10^{10}	2.34×10^{10}	2.67×10^{10}	6.50×10^{10}
2a	1.17×10^{10}	1.54×10^{10}	1.22×10^{10}	9.29×10^9	7.09×10^9	2.49×10^9	9.40×10^9	1.96×10^9
1a	1.05×10^{10}	9.49×10^9	1.11×10^{10}	9.67×10^9	7.21×10^9	1.55×10^9	4.11×10^9	3.12×10^9
1b	8.48×10^9	4.75×10^9	3.94×10^9	1.04×10^{10}	8.48×10^9	4.75×10^9	3.94×10^9	1.04×10^{10}
3c	8.11×10^9	4.53×10^9	3.76×10^9	5.24×10^9	8.11×10^9	4.53×10^9	3.76×10^9	5.24×10^9
2b	6.20×10^9	3.58×10^9	2.88×10^9	6.32×10^9	6.33×10^9	3.54×10^9	2.97×10^9	6.32×10^9

Specific resistivity ρ calculated from the van der Pauw method; sample thickness: 0.42 mm Exp 1; 2.35 mm Exp 2; 1.95 mm Exp3; 2.95 mm Exp4; setup: (1a; 1b) SMU 2450 in the constant current (1 nA; 2 nA) and measure voltage mode; (2a, 2b) SMU 2450 in the constant voltage (5 V; 10 V) and measure current mode; (3a, 3b, 3c) electrometer 6517B as a voltage source and an ammeter (5 V; 10 V; 20 V) and SMU 2450 as a voltmeter

perovskite material in the vicinity of the electrode at 100 V cannot be excluded.

For all samples, the I-V curves in both scan directions are characterised by fluctuations in the mid-to high-voltage range. Several possible explanations for the observed variation in current behavior exist. It can be attributed to drift and diffusion of charge carriers including migration of Br$^-$ anions and their accumulation at an anode and a cathode (saturation current). Other accounts include surface-conductivity effect of the two opposite crystal faces that are characterised by different growth features and defects such as V_{Br} and Bi_{Ag}, linear dislocations causing abrupt change in atomic arrangement, twin planes, cracks and inclusions including precipitates. According to these data, we can infer that nature of the samples and electrodes has a strong bearing on the character of the I-V curves.

There are a number of important similarities and differences between the SCLC and Hall-effect measurements. Both measurements are influenced by the type of the electrodes (carbon and Ag) and both have
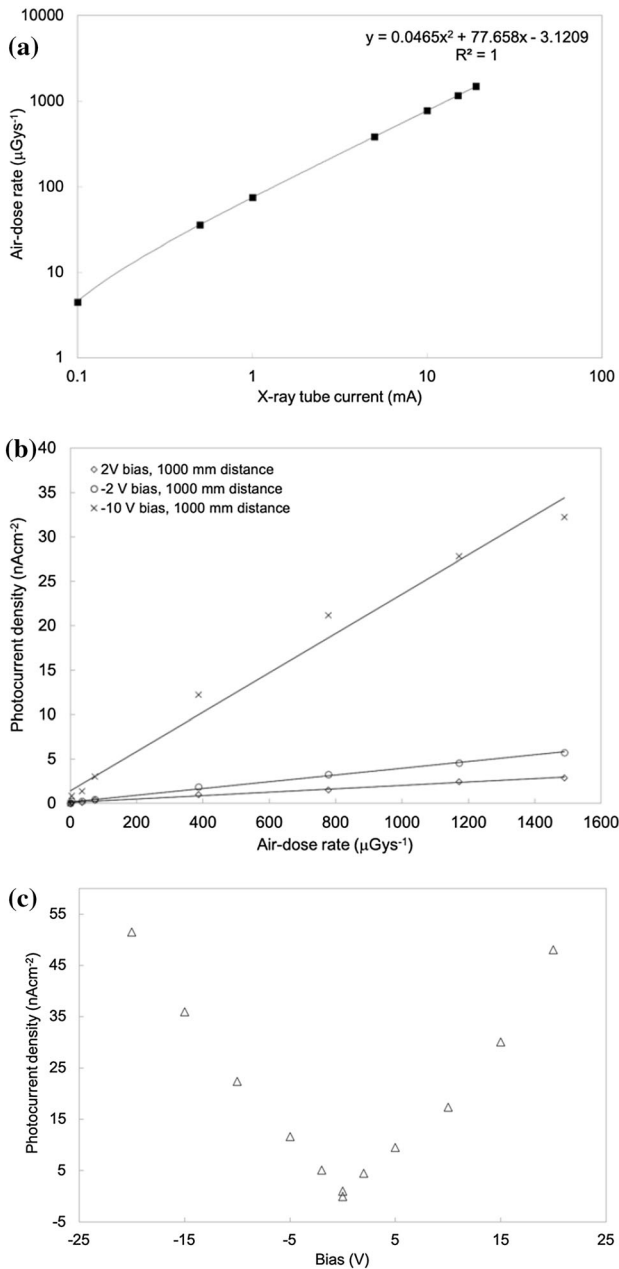
Figure 6 A calibration data plot (**a**). Dependence of the photocurrent density on the dose rate at + 2 V, − 2 V, and − 10 V bias for the Exp4 sample-to-source separation of 1000 mm (**b**). Relationship between the Exp4 sample photocurrent density and the sample bias determined at 5 mA X-ray tube current and the sample-to-source separation of 1000 mm (**c**). The sample area was estimated to 0.25 cm^2.

limitations in derivation of the μ. The SCLC method is used to record current flowing between two electrodes deposited on the opposite crystal surfaces as a function of applied bias. Limitation of the SCLC method is in a clear definition of the SCLC regime

reached higher voltages. But, the *I-V* curves rarely exhibit the three well-defined regimes (the ohmic, trap-filled, and trap-free regimes). Using μ value derived in the space-charge-limited regime and the ρ value derived in the ohmic regime to calculate the charge carrier concentration can be misleading because each regime is characterised by a specific behavior of charge carriers depending on applied bias [29, 30]. On the other hand, the Hall-effect measurements involve measurements of current and voltage across the crystal (between diagonal contacts, for example AC current and DB voltage). Limitation of the Hall effect in van der Pauw geometry is in deflection of charge carriers in a magnetic field and ρ calculated from the van der Pauw measurements of current and voltage along the edges of a crystal surface (for example, AB current and DC voltage). The preliminary Hall-effect measurements indicate that the Exp4 sample is a p-type semiconductor in case of both Ag and carbon paint electrodes with a narrow range of μ values 1.89–2.36 cm^{2}V^{-1} s^{-1}. An improved setup is required to confirm these values and investigate the remaining samples.

In case of the van der Pauw measurements, unsymmetrical growth zones and defects are also the cause of the mismatch in the current and voltage values measured for reversed polarities. Nevertheless, the ρ values for both the Ag-Cs$_2$AgBiBr$_6$-Ag and the carbon-Cs$_2$AgBiBr$_6$-carbon configurations are on the order of 10^{10} Ωcm, with the maximum value of 6.65×10^{10} Ωcm, are within the range of the published values especially [7] and [8] (Table 4). Although the ρ data obtained in the SCLC method (carbon 10^6–10^8 Ωcm and Ag 10^8–10^9 Ωcm) and the van der Pauw (carbon 10^9 Ωcm and Ag 10^9–10^{10} Ωcm) were measured using the 2450 Keithley instrument, they differ on the order of 10^1 Ωcm. This rather contradictory result can be explained in terms of the measurement procedure as discussed earlier and nature of the samples. The rims being more resistive along the pseudo-hexagonal crystals face, while the center of a sample, where the seed is located, is more conductive, due to higher density of defects and strained lattice. With respect to n_{trap}, the current values of 10^{10} cm^{-3} are mostly in agreement with the [24] and [25] (Table 4).

The X-ray photoresponse of the sample Exp4 was investigated in terms of the dependence of photocurrent density on the applied bias, the X-ray tube

Table 4 Key electrical parameters for the $Cs_2AgBiBr_6$ single crystals derived from the SCLC method including radiation performance parameters

Electrodes	$\rho(\Omega cm)$	$V_{TFL}(V)$	μ (cm²V⁻¹s⁻¹)	n_{trap}(cm⁻³)	Sensitivity (μCGy_{air}^{-1} cm⁻²)	Dose rate (nGy$_{air}$s⁻¹)
Au/pristine sample [7]	10^9		3.17	4.54×10^9		
Au/annealed sample [7]	10^{11}		11.81	1.74×10^9	105	59.7
Ag/pristine sample [24]		3.48	0.49	3.58×10^{10}		
Au/natural cooling sample [8]	1.51×10^9		1.70			
Au/controlled cooling sample [8]	1.35×10^{10}		10.8		1974	45.7
Au/pristine sample [9]		5.18	2.25	6.04×10^9	165.5	
Pristine sample [10]					316	
Pristine sample [28]	8.33×10^9	5.02		1.16×10^9		
Au/pristine sample [25]	5.40×10^9	52.4	7.02	1.44×10^{10}		

Space-charge limit current SCLC method; resistivity ρ; trap-filled limit voltage V_{TFL}; charge carrier mobility μ; density of trap states n_{trap}. The charge carrier mobility-lifetime product $\mu\tau$ for a crystal grown using the controlled cooling method is 5.95×10^{-3} cm² V⁻¹ and for a crystal grown using the natural cooling method is 1.36×10^{-4} cm² V⁻¹ [8]; $\mu\tau$ of 2.48×10^{-3} cm² V⁻¹ [25]

current, and the source-sample distance. Its calculated maximum sensitivity of 42 μCGy_{air}^{-1} cm⁻² at a dose rate of 75 μGys^{-1} and −10 V bias is in good agreement with Pan et al. [7], who reported 50 μCGy_{air}^{-1} cm⁻² at 10 V bias. This study, therefore, indicates that the synthesized $Cs_2AgBiBr_6$ samples satisfy requirements for radiation sensors.

Further advances in the *I-V* measurements such as developing an in-house program that controls the measurements are necessary to more accurately assess the importance of source delay time and interval times between scan directions. Thermal annealing and optimisation of metal–semiconductor contacts can in future lead to enhanced performance of the double perovskite-based detector devices. Recently, it has been revealed that the self-trapping process is less severe at room T and can be tuned through electronic dimensionality and composition [19]. Hence, future studies will focus on investigating crystal growth and characterization of 2D layered $(BA)_2CsAgBiBr_7$ double perovskite material.

Conclusion

This work contributes to existing knowledge of $Cs_2AgBiBr_6$ radiation sensors by providing additional information on the crystal microstructures, electrical characterisation, and X-ray photoresponse measurements. As evidenced from investigation of microstructure, the advanced crystal growth has produced larger single crystals of $Cs_2AgBiBr_6$ with enhanced crystalline quality and improved electrical performances. The powder XRD measurement has verified the purity and crystallinity of the $Cs_2AgBiBr_6$ samples with cubic symmetry ($Fm\overline{3}m$). The single-crystal XRD patterns reveal the dominant {111} lattice planes parallel to the sample surface. The van der Pauw ρ values of 1.55×10^9–6.65×10^{10} Ωcm are typically higher for the Ag electrodes and suggest an improved electrical performance compared to that of the carbon electrodes. The ρ values, the Hall effect, and SCLC estimated μ values including the n_{trap} values are comparable with the published data. The key electrical parameters and the initial X-ray photoresponse measurements yielding the maximum sensitivity of 42 $\mu CGyair^{-1}$ cm⁻² at a dose rate of 75 μGys^{-1} and −10 V bias indicate that the $Cs_2AgBiBr_6$ samples satisfy requirements for radiation sensors.

Author contributions

Funding

Declarations

References

[1] Wei H, Fang Y, Mulligan P et al (2016) Sensitive X-ray detectors made of methylammonium lead tribromide perovskite single crystals. Nat Photonics 10:333–339

[2] Li L, Liu X, Zhang H et al (2019) Enhanced X-ray sensitivity of MAPbBr$_3$ detector by tailoring the interface-states density. ACS Appl Mater Interf 11:7522–7528. https://doi.org/10.1021/acsami.8b18598

[3] Geng X, Feng Q, Zhao R et al (2020) High-quality single crystal perovskite for highly sensitive X-ray detector. IEEE Electron Device Lett 41:256–259. https://doi.org/10.1109/LED.2019.2960384

[4] Xu Q, Shao W, Li Y et al (2019) High-performance surface barrier X-ray detector based on methylammonium lead tribromide single crystals. ACS Appl Mater Interf 11:9679–9684. https://doi.org/10.1021/acsami.8b21605

[5] Ye F, Lin H, Wu H et al (2019) High-quality cuboid CH$_3$NH$_3$PbI$_3$ single Crystals for high performance X-ray and photon detectors. Adv Funct Mater 29:1806984–1806991. https://doi.org/10.1002/adfm.201806984

[6] Murgulov V, Daub M, Hillebrecht H et al (2020) Growth and characterization of radiation sensors based on single crystals of hybrid metal-organic methylammonium lead bromide and iodide perovskite. Cryst Res Technol 55:2000112–2000123. https://doi.org/10.1002/crat.202000112

[7] Pan W, Wu H, Luo J et al (2017) Cs$_2$AgBiBr$_6$ single-crystal X-ray detectors with a low detection limit. Nat Photonics 11:726–732. https://doi.org/10.1038/s41566-017-0012-4

[8] Yin L, Wu H, Pan W et al (2019) Controlled cooling for synthesis of Cs$_2$AgBiBr$_6$ single crystals and its application for X-ray detection. Adv Opt Mater 7:1900491–1900498. https://doi.org/10.1002/adom.201900491

[9] Yuan W, Niu G, Xian Y et al (2019) In situ regulating the order-disorder phase transition in Cs$_2$AgBiBr$_6$ single crystal toward the application in an X-ray detector. Adv Funct Mater 29:1900234–1900242. https://doi.org/10.1002/adfm.201900234

[10] Zhang H, Gao Z, Liang R et al (2019) X-ray detector based on all-inorganic lead-free Cs$_2$AgBiBr$_6$ perovskite single crystal. IEEE Trans Electron Devices 66:2224–2229. https://doi.org/10.1109/TED.2019.2903537

[11] Su Y, Ma W, Yang YM (2020) Perovskite semiconductors for direct X-ray detection and imaging. J Semicond 41:051204. https://doi.org/10.1088/1674-4926/41/5/051204

[12] Wu H, Ge Y, Niu G, Tang J (2021) Metal halide perovskites for X-ray detection and imaging. Matter 4:144–163. https://doi.org/10.1016/j.matt.2020.11.015

[13] Vasala S, Karppinen M (2015) $A_2B'B''O_6$ perovskites: a review. Prog Solid State Chem 43:1–36. https://doi.org/10.1016/j.progsolidstchem.2014.08.001

[14] McClure ET, Ball MR, Windl W, Woodward PM (2016) Cs_2AgBiX_6 (X = Br, Cl): new visible light absorbing, lead-free halide perovskite semiconductors. Chem Mater 28:1348–1354. https://doi.org/10.1021/acs.chemmater.5b04231

[15] Slavney AH, Hu T, Lindenberg AM, Karunadasa HI (2016) A bismuth-halide double perovskite with long carrier recombination lifetime for photovoltaic applications. J Am Chem Soc 138:2138–2141. https://doi.org/10.1021/jacs.5b13294

[16] Xiao Z, Meng W, Wang J, Mitzi DB, Yan Y (2017) Searching for promising new perovskite-based photovoltaic absorbers: the importance of electronic dimensionality. Mater Horiz 4:206–216. https://doi.org/10.1039/C6MH00519E

[17] Hutter EM, Gélvez-Rueda MC, Bartesaghi D, Grozema FC, Savenije TJ (2018) Band-like charge transport in $Cs_2AgBiBr_6$ and mixed antimony-bismuth $C_{s2}AgBi_{1-x}Sb_xBr_6$ halide double perovskites. ACS Omega 3:11655–11662. https://doi.org/10.1021/acsomega.8b01705

[18] Buizza LRV, Herz LM (2021) Polarons and charge localization in metal-halide semiconductors for photovoltaic and light-emitting devices. Adv Mater 33:2007057. https://doi.org/10.1002/adma.202007057

[19] Wright AD, Buizza LRV, Savill KJ, Longo G, Snaith HJ, Johnston MB, Herz LM (2021) Ultrafast excited-state localization in $Cs_2AgBiBr_6$ double perovskite. J Phys Chem Lett 12:3352–3360. https://doi.org/10.1021/acs.jpclett.1c00653

[20] Li T, Zhao X, Yang D et al (2018) Intrinsic defect properties in halide double perovskites for optoelectronic applications. Phys Rev Appl 10:041001–0410012. https://doi.org/10.1103/PhysRevApplied.10.041001

[21] Xiao Z, Meng W, Wang J, Yan Y (2016) Thermodynamic stability and defect chemistry of bismuth-based lead-free double perovskites. Chemsuschem 9:2628–2633. https://doi.org/10.1002/cssc.201600771

[22] Zhang Z, Cao D, Huang Z, Danilov EO, Chung C-C, Sun D, Yang G (2021) Gamma-ray detection using Bi-poor $Cs_2AgBiBr_6$ double perovskite single crystals. Adv Opt Mater 9:2001575–2001580. https://doi.org/10.1002/adom.202001575

[23] Delor M, Slavney AH, Wolf NR, Filip MR, Neaton JB, Karunadasa HI, Ginsberg NS (2020) Carrier diffusion lengths exceeding 1 μm despite trap-limited transport in halide double perovskites. ACS Energy Lett 5:1337–1345. https://doi.org/10.1021/acsenergylett.0c00414

[24] Dang Y, Tong G, Song W et al (2020) Interface engineering strategies towards $Cs_2AgBiBr_6$ single-crystalline photodetectors with good Ohmic contact behaviours. J Mater Chem C 8:276–284. https://doi.org/10.1039/C9TC04780H

[25] Zhang Z, Chung C-C, Huang Z et al (2020) Towards radiation detection using $Cs_2AgBiBr_6$ double perovskite single crystals. Mater Lett 269:127667–127670

[26] Le Corre VM, Duijnstee EA, El Tambouli O et al (2021) Revealing charge carrier mobility and defect densities in metal halide perovskites via space-charge-limited current measurements. ACS Energy Lett 6:1087–1094. https://doi.org/10.1021/acsenergylett.0c02599

[27] Duijnstee EA, Ball JM, Le Corre VM et al (2020) Toward understanding space-charge limited current measurements on metal halide perovskites. ACS Energy Lett 5:376–384. https://doi.org/10.1021/acsenergylett.9b02720

[28] Zhang W, Zhu H, Pan S et al (2020) Growth and properties of centimeter-sized lead free all inorganic perovskite $Cs_2AgBiBr_6$ crystal by additive $C_H3COONa$. J Cryst Growth 532:125440. https://doi.org/10.1016/j.jcrysgro.2019.125440

[29] Röhr JA, Kirchartz T, Nelson J (2017) On the correct interpretation of the low voltage regime in intrinsic single-carrier devices. J Phys Condens Matter 29:205901. https://doi.org/10.1088/1361-648x/aa66cc

[30] Röhr JA, Moia D, Haque SA et al (2018) Exploring the validity and limitations of the Mott-Gurney law for charge-carrier mobility determination of semiconducting thin-films. J Phys Condens Matter 30:105901–105918. https://doi.org/10.1088/1361-648x/aaabad

[31] Röhr JA (2019) Direct determination of built-in voltages in asymmetric single-carrier devices. Phys Rev Appl 11:054079–054088. https://doi.org/10.1103/PhysRevApplied.11.054079

[32] Lampert MA (1956) Simplified theory of space-charge-limited currents in an insulator with traps. Phys Rev 103:1648–1656. https://doi.org/10.1103/PhysRev.103.1648

[33] Lampert MA, Mark P (1970) Current injections in solids. Electrical current series. Academic Press, p 354